Supplementary Information

FG-Nup Sequence Length Polydispersity Enhances Selectivity of Nuclear Pore Complex Translocation

Manoj K Patel[1], Lokesh Soni[1] and Ajay S Panwar[1]*

[1]Department of Metallurgical Engineering and Materials Science,

Indian Institute of Technology Bombay, Powai, Mumbai 400076, India

*Corresponding author: panwar@iitb.ac.in

Table of Contents **Page**

S1. Geometry Optimization and Brush Equilibration		S4
S2. Radius of gyration, density distribution, and chain polydispersity		S5
Figure S1.	Characterization of grafted FG-Nup brush conformations	S6
Figure S2.	Characterization of grafted FG-Nup brush conformations	S7
Figure S3.	Left, middle, and right column plot shows equilibrated density distributions of different pore setups along the axial direction, in radial direction inside the cylinder, and in radial direction outside the cylinder, respectively.	S8
Figure S4.	Plots showing *sy*-tracer's transport probabilities associated with tracer translocation as function of f	S9
Figure S5.	Inert tracer trajectories from twenty independent simulations through homogeneous pore shown for different values of f	S10
Figure S6.	Distributed patchy tracer trajectories from twenty independent simulations through homogeneous pore shown for different values of f (	S11
Figure S7.	Dense patchy tracer trajectories from twenty independent simulations through homogeneous pore shown for different values of f	S12
Figure S8.	Inert patchy tracer trajectories from twenty independent simulations through inhomogeneous pore shown for different values of f	S13
Figure S9.	Distributed patchy tracer trajectories from twenty independent simulations through inhomogeneous pore shown for different values of f	S14
Figure S10.	Dense patchy tracer trajectories from twenty independent simulations through inhomogeneous pore shown for different values of f	S15
Figure S11.	Plots showing the equilibrated density distributions of polymer brush segments, considering both hydrophobic and hydrophilic segments.	S16
Figure S12.	Plots showing the equilibrated density distributions of polymer brush segments, considering only hydrophilic segments.	S17
Figure S13.	Plots showing the equilibrated density distributions of polymer brush segments, considering both hydrophobic and hydrophilic segments.	S18
Figure S14.	Plots showing the equilibrated density distributions of polymer brush segments, considering only hydrophilic segments.	S19

Figure S15.	Denser patchy tracer trajectories from twenty independent simulations through homogeneous pore shown for different values of f after weakening of tracer-FG hydrophobic affinity.	S20
Figure S16.	Dense patchy tracer trajectories from twenty independent simulations through inhomogeneous pore shown for different values of f after weakening of tracer-FG hydrophobic affinity.	S21
Figure S17.	Final probabilities associated with different tracer translocation as function of f after weakening hydrophobic interaction between *hd*-tracer and middle rings.	S22
Figure S18.	Average number of binding contacts, $\langle n_b \rangle$, between tracer binding domains and FG-repeats corresponding to individual rings, $R1 - R9$, shown for both *h*-NPC and *ih*-NPC at $f = 0.1$ and $f = 0.2$.	S23
Figure S19.	Hydrophobic binding contacts between the $sy-$tracer (distributed patchy tracer) and FG-Nups at $f = 0.2$, during its passage through the *ih*-NPC (inhomogeneous pore).	S24
Figure S20.	Hydrophobic binding contacts between the *sy*-tracer (distributed patchy tracer) and FG-Nups at $f = 0.2$, during its passage through the *h*-NPC (homogeneous pore).	S25
Figure S21.	Hydrophobic binding contacts between the *hd*-tracer (denser patchy tracer) and FG-Nups at $f = 0.2$, during its passage through the *h*-NPC (homogeneous pore).	S26

S1. Geometry Optimization and Brush Equilibration

Before tracer-transport simulations were performed, the FG-Nup assemblies inside the cylindrical pore were relaxed to obtain equilibrated polymer-brush conformations. Each random copolymer chain was first generated in a stretched configuration along the pore wall to avoid bead overlap. The system was then subjected to an initial energy-minimization step using the steepest-descent algorithm implemented in LAMMPS, which removes unphysical bead contacts and relaxes strained bonds.

Following minimization, the brushes were equilibrated using Langevin dynamics at a temperature of 310 K for a duration of 200×10^6 timesteps for all the hydrophobic fraction f. During this stage, the FG-Nups were allowed to evolve freely while keeping the grafting points fixed. No tracers were present during equilibration. Convergence was assessed by monitoring the radial density distributions of polymer beads. These quantities plateaued in the equilibration window, indicating that the brushes had reached a steady conformational state.

After equilibration, the final polymer configurations were used as starting structures for all transport simulations. The same relaxation protocol was applied to both the homogeneous NPC ($h-$NPC) containing chains of length $N = 300$ and the inhomogeneous NPC ($ih-$NPC) with mixed FG-Nup lengths having $N = 200$ for middle 3 rings and $N = 300$ for rest peripheral rings. This ensures that all tracer-transport trajectories begin from well-minimized and equilibrated initial configurations.

S2. Radius of gyration, density distribution, and chain polydispersity

To characterize the conformations of the grafted FG-Nup brushes, we computed the radius of gyration, R_g, for every grafted chain in the following pore architectures for three hydrophobic fractions, $f = 0.1, 0.2, 0.3$,

- Homogeneous pore ($h-$NPC, $N = 300$)
- Homogeneous pore ($h-$NPC, $N = 200$)
- Inhomogeneous pore ($ih-$NPC)

For each case we analyzed the last 1×10^6 timesteps of the equilibrated brush and obtained time-averaged R_g values for every chain.

The chain-resolved R_g values (Figure S1A) show the expected trends. For a fixed hydrophobic fraction f, the shorter chains with $N = 200$ systematically exhibited smaller R_g values. Whereas, longer chains with $N = 300$ showed the largest R_g values, chains in the $ih-$NPC (short chains in the middle rings, $N = 200$, and long chains at the periphery, $N = 300$) displayed intermediate R_g values. The R_g values for the $ih-$NPC are "sandwiched" between the two monodisperse cases. As f increased from 0.1 to 0.3, R_g values decreased for all three architectures, consistent with increased attractive FG–FG cohesion and a more compact brush.

We also constructed normalized probability distributions of R_g over all chains over the same time window (Figure S1B). These distributions were single-peaked and relatively narrow for both $N = 200$ and $N = 300$, indicating a well-defined brush state rather than the coexistence of distinct swollen and collapsed subpopulations. The distributions clearly showed that $ih-$NPC architecture corresponded to R_g values intermediate to the $N = 200$ and $N = 300$ $h-$NPC architectures.

In all cases the chains strongly overlapped within the pore, forming a dense brush-like network. Outside the pore the chains were in a stretched state (shown in snapshots in Figure 1 and density distributions in Figure 5). Our coarse-grained bead–spring model enforces excluded volume and connectivity. The chains mostly form transient hydrophobic FG-FG contacts (physical cross-links) inside the pore resulting in a hydrogel network. These aspects were discussed extensively in our previous paper.[1] Although, entanglements are probably possible, their investigation is beyond the

scope of the current paper. . The R_g characterization therefore confirmed that the grafted polymers form an overlapping brush network whose conformations evolve in a manner consistent with the expected dependence on chain length and hydrophobic fraction.

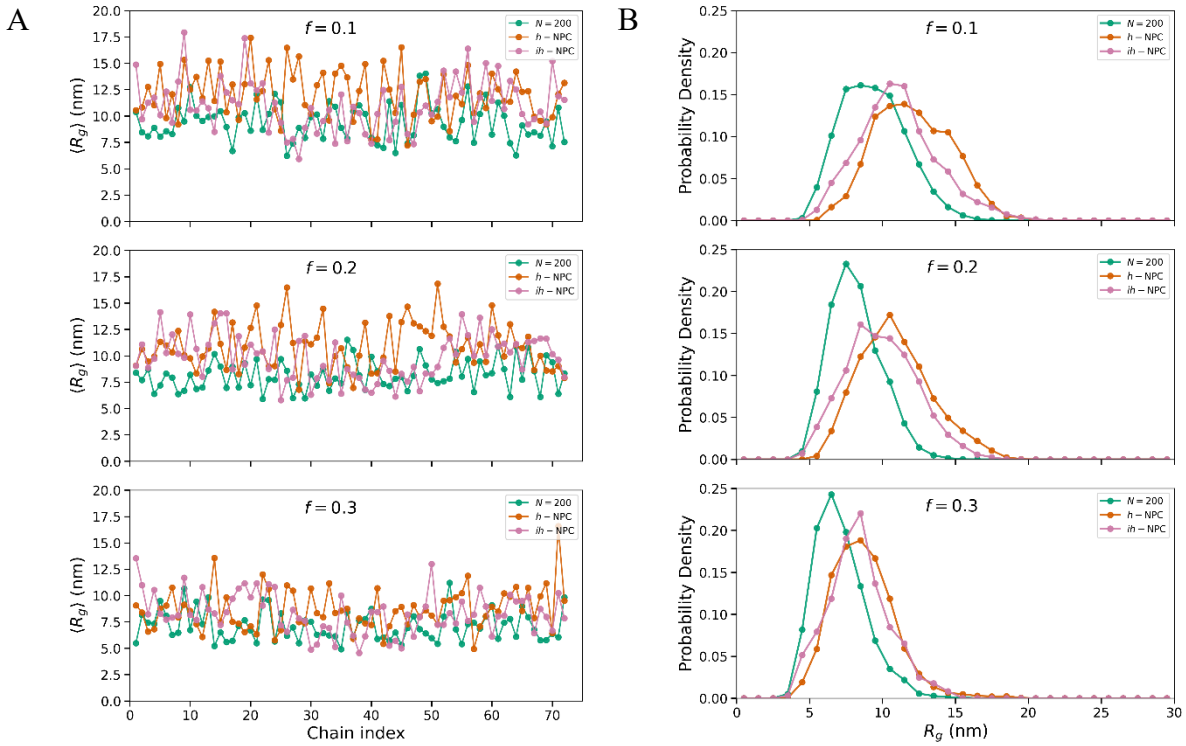

Figure S1. Characterization of grafted FG-Nup brush conformations. (A) Normalized probability distributions of R_g for the different pore setup and values of f. The distributions are single-peaked and shift to lower R_g with increasing f, reflecting increased FG–FG cohesion and brush compaction. Overall, the chains form a dense, overlapping brush-like network within the pore. (B) Time-averaged radius of gyration $\langle R_g \rangle$ for each grafted chain as a function of chain index, for $N = 200$ (green), $N = 300$ (h −NPC, orange), inhomogeneous pore (ih −NPC, magenta) and the polydisperse pore (blue) at three hydrophobic fractions $f = 0.1$,0.2 and 0.30. Data are averaged over the last 1×10^6 simulation timesteps of the equilibrated brush. For a given f, shorter chains ($N = 200$) exhibit smaller R_g, longer chains ($N = 300$) exhibit larger R_g, and the ih −NPC lies in between.

Another pore architecture (referred to as the "polydisperse pore") was constructed with linearly varying values of N for the polymer chains grafted inside the pore. The grafted polymer, FG-Nup, chain lengths decreased linearly from $N = 300$ at the outermost ring R1 (or R9) to $N = 200$ at the middle ring R5.

The R_g values and their distributions for the polydisperse pore were very similar to those of the ih −NPC (see Figure S2). Density distributions of polydisperse pore showed trends like both h − NPC and ih − NPC (Figure S3). Since the architecture of the polydisperse pore is closer to that of ih − NPC, the translocation behaviour of tracers is expected to be like ih −NPC.

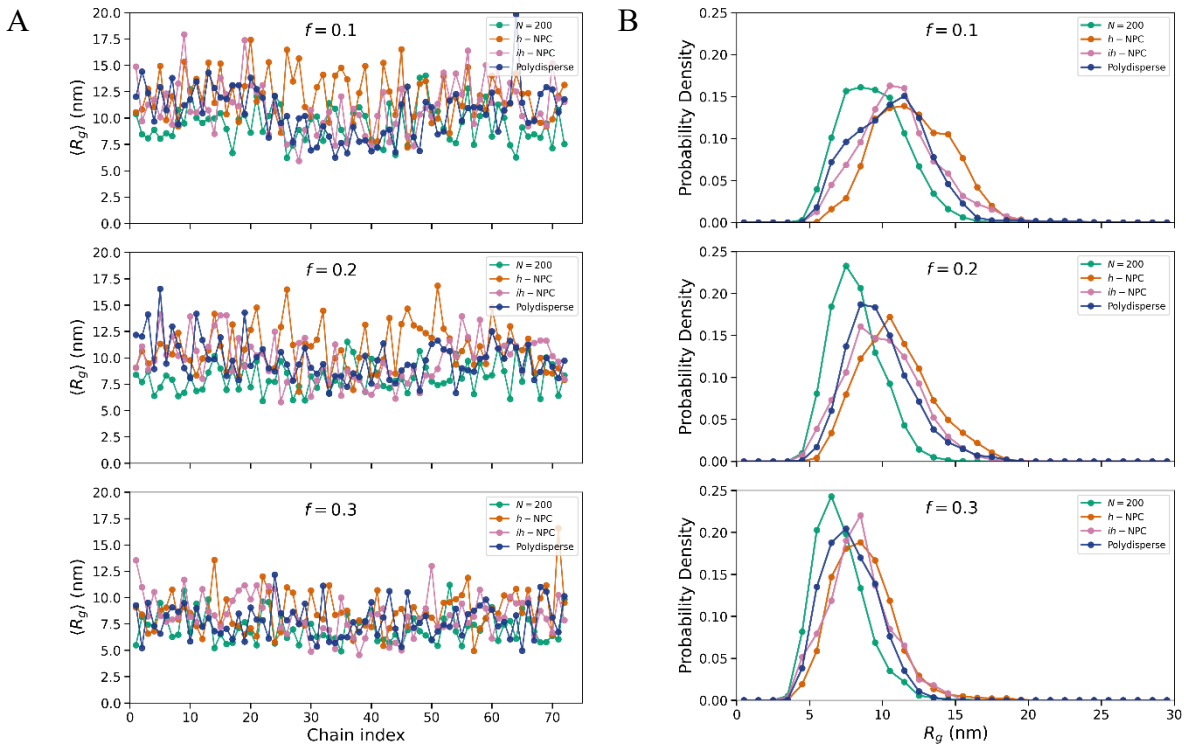

Figure S2. Characterization of grafted FG-Nup brush conformations. (A) Normalized probability distributions of R_g for the different pore setup and values of f. The distributions are single-peaked and shift to lower R_g with increasing f, reflecting increased FG–FG cohesion and brush compaction. Overall, the chains form a dense, overlapping brush-like network within the pore. (B) Time-averaged radius of gyration $\langle R_g \rangle$ for each grafted chain as a function of chain index, for $N = 200$ (green), $N = 300$ (h −NPC, orange), inhomogeneous pore (ih −NPC, magenta) and the polydisperse pore (blue) at three hydrophobic fractions $f = 0.1$,0.2 and 0.30. Data are averaged over the last 1×10^6 simulation timesteps of the equilibrated brush. For a given f, shorter chains ($N = 200$) exhibit smaller R_g, longer chains ($N = 300$) exhibit larger R_g, and the ih −NPC lies in between.

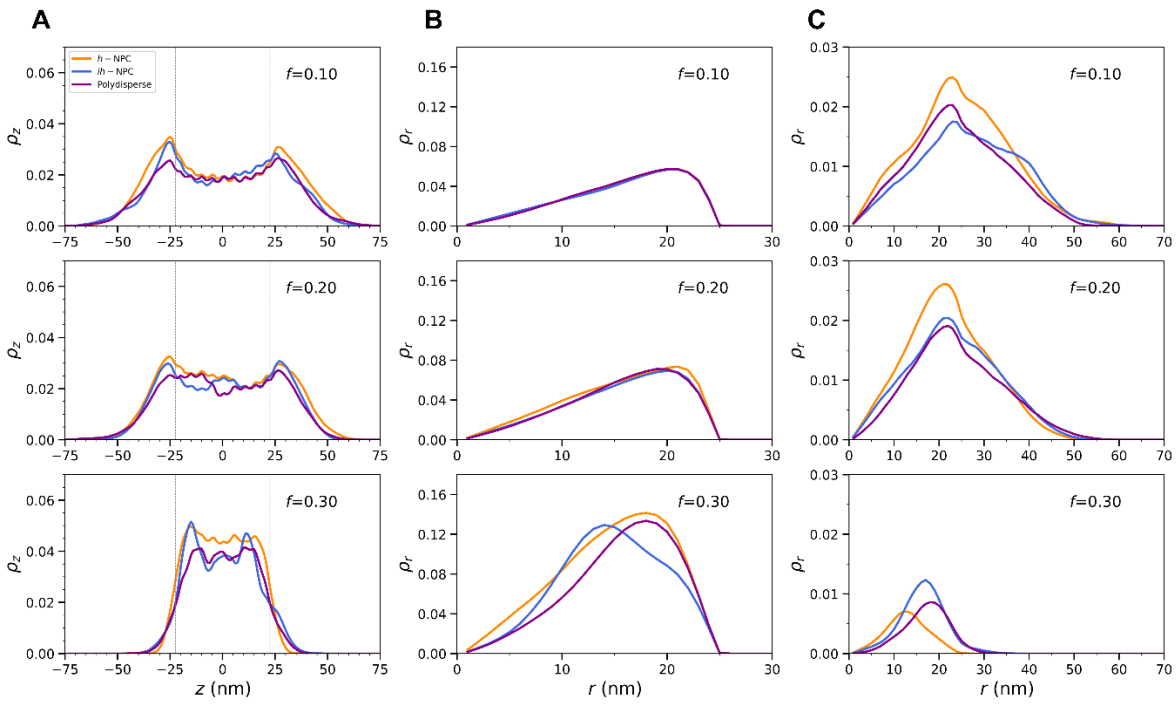

Figure S3. Left, middle, and right column plot shows equilibrated density distributions of different pore setups along the axial direction, in radial direction inside the cylinder, and in radial direction outside the cylinder, respectively.

The translocation of the sy −tracer was simulated through the polydisperse pore to understand the effect of polydispersity on pore selectivity. Ten trajectories each were simulated for $f = 0.1, 0.2, 0.3$ (see Figure S4A) and the probabilities of entry, crossing mid-plane and passage (p_e, p_m, and p_s, respectively) were calculated (Figure S4B). All three probabilities were very close to the respective probability values for the sy −tracer translocating through the ih −NPC (see Figures 3D-F). The maximum p_s values were observed for $f = 0.2$, consistent with the results from the previous study with ih − NPC and the current work with ih − NPC. For $f = 0.3$, the sy −tracer was observed to bounce off the collapsed brush formed inside the pore (very close to the entry) due the large number of hydrophobic interactions. This cluster of collapsed polymer chains (shown in Figures S4C, D) made tracer translocation difficult through the pore. As a result, the sy −tracer remained stuck at the pore entry.

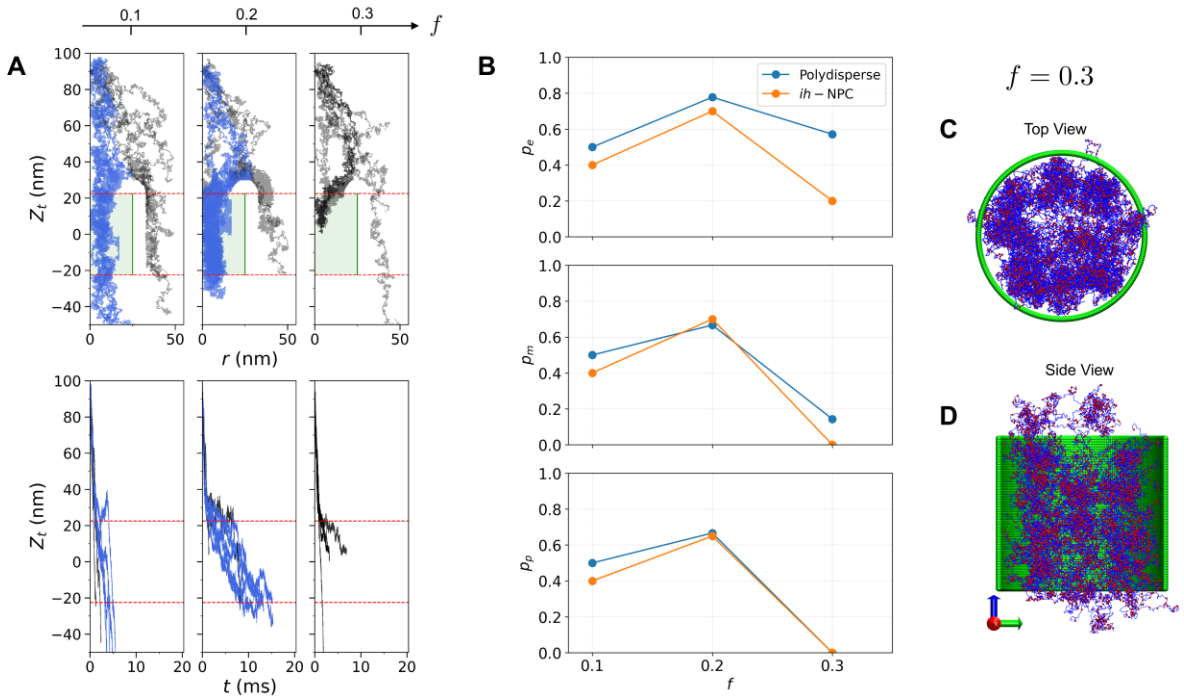

Figure S4. (A) Plots showing *sy*-tracer's transport probabilities associated with tracer translocation as function of f, including the probability of tracer entry, p_e, probability of crossing the NPC mid-plane, p_m, and the probability of the tracer completely exiting the pore, p_p. (B) Trajectories of sy −tracer through pore (green), successful passage marked as blue and rejected one coloured as black trajectories. (C) Side and top view of polydisperse pore.

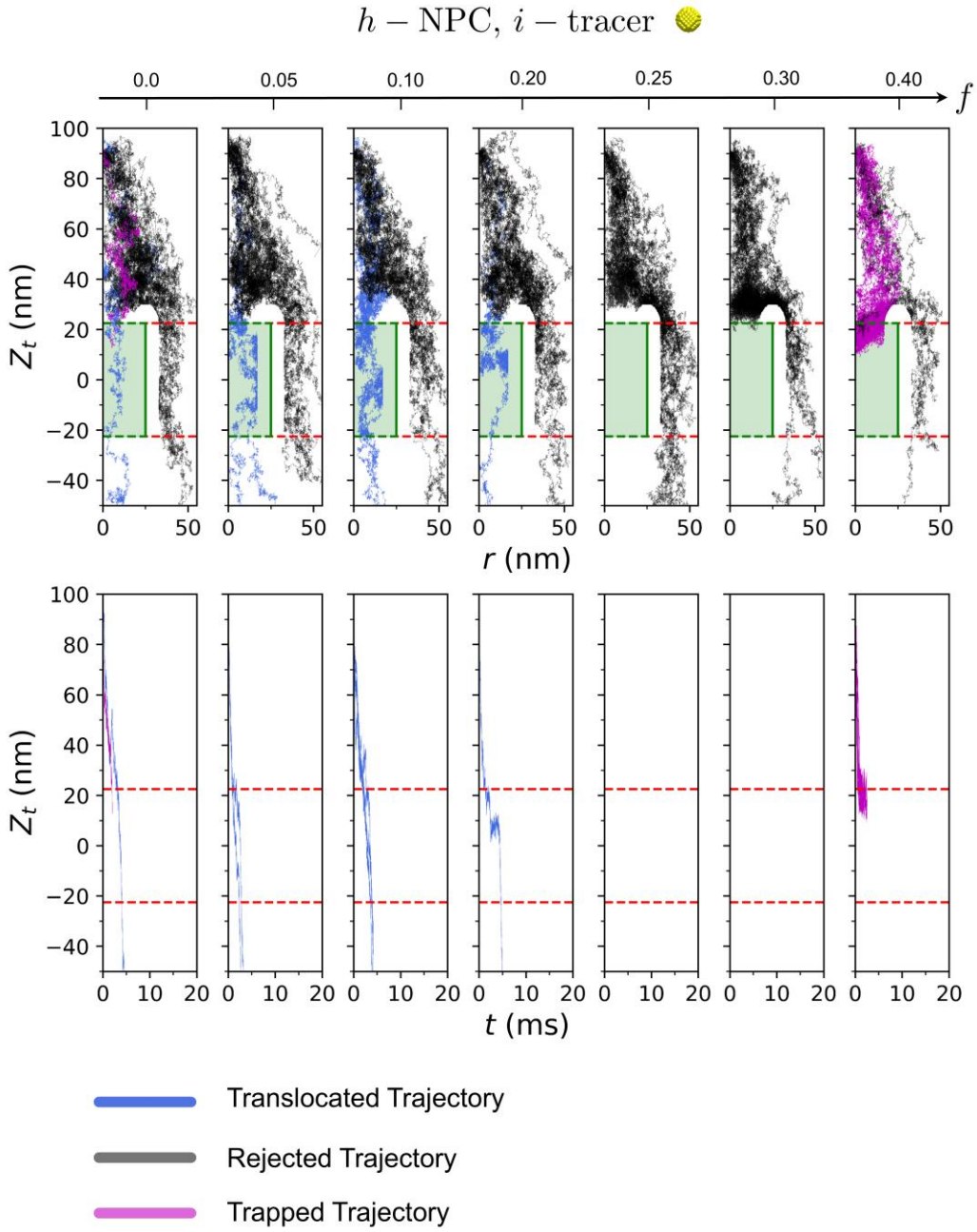

Figure S5. Inert tracer trajectories from twenty independent simulations through homogeneous pore shown for different values of f (A) Tracer paths during the simulations represented as Z_t vs r plots, where Z_t is the z-coordinate of the tracer, and r is tracer radial coordinate. (B) Plots showing the variation of Z_t with time t.

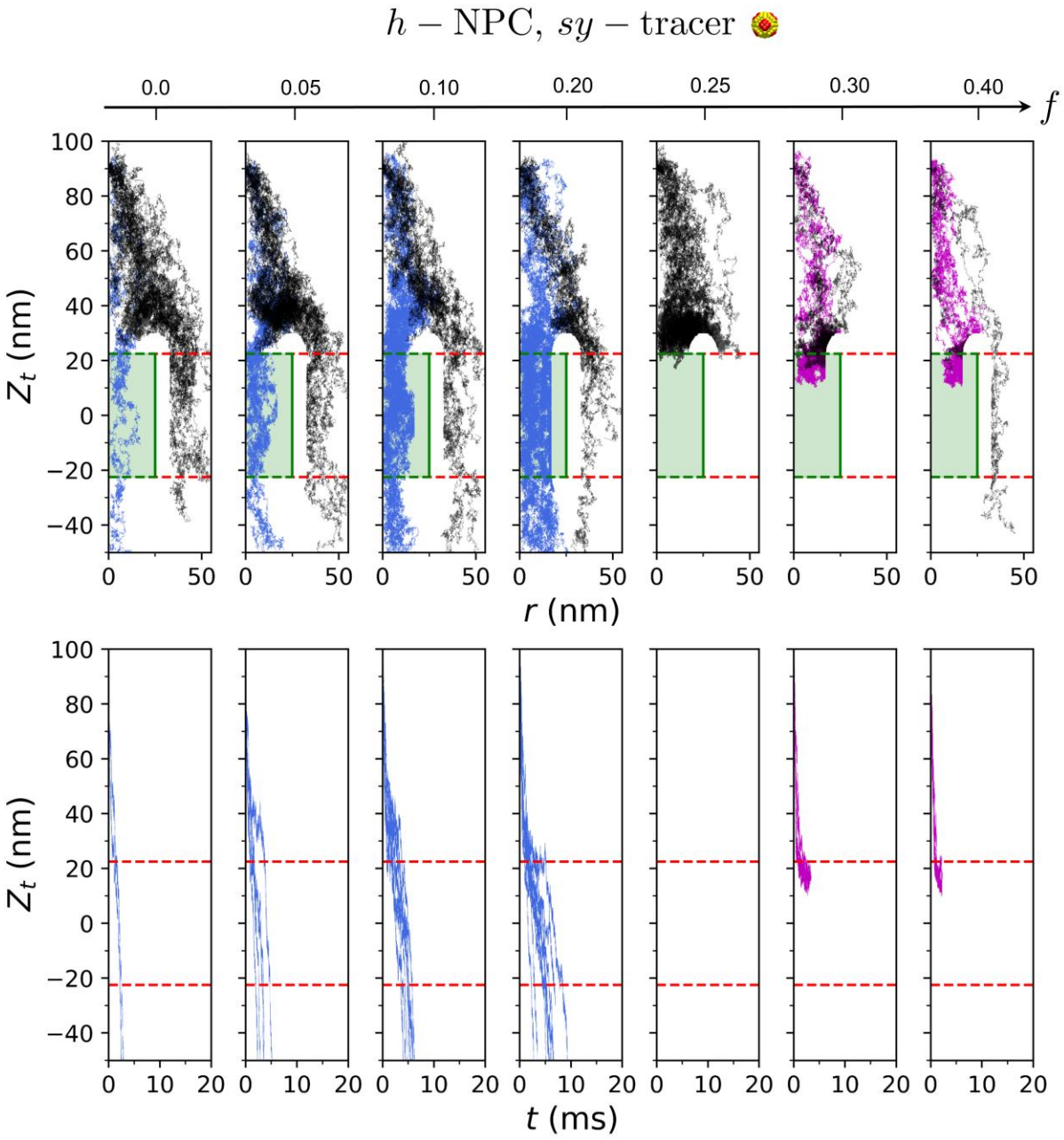

Figure S6. Distributed patchy tracer trajectories from twenty independent simulations through homogeneous pore shown for different values of f (A) Tracer paths during the simulations represented as Z_t vs r plots, where Z_t is the z-coordinate of the tracer, and r is tracer radial coordinate. (B) Plots showing the variation of Z_t with time t.

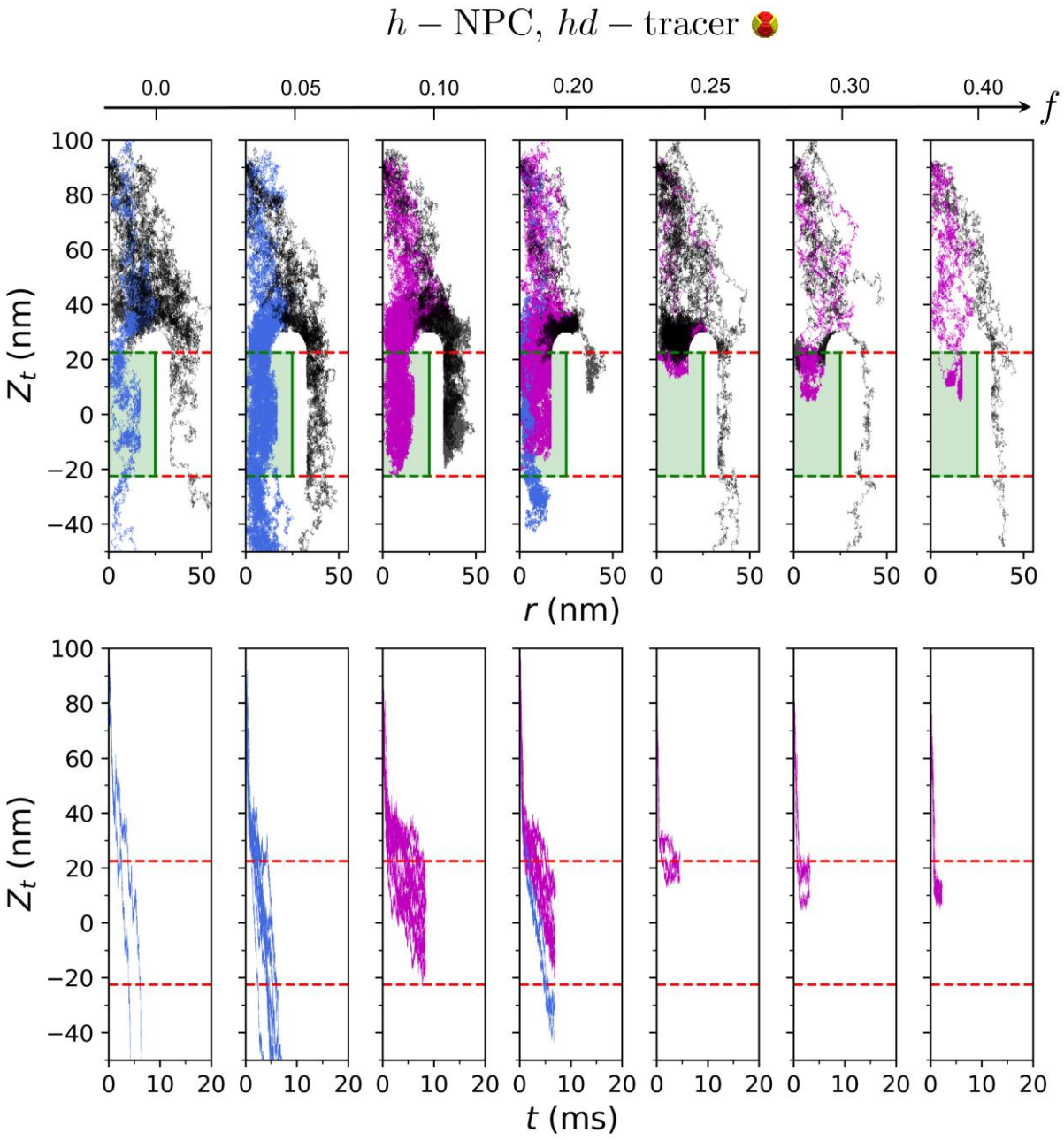

Figure S7. Dense patchy tracer trajectories from twenty independent simulations through homogeneous pore shown for different values of f (A) Tracer paths during the simulations represented as Z_t vs r plots, where Z_t is the z-coordinate of the tracer, and r is tracer radial coordinate. (B) Plots showing the variation of Z_t with time t.

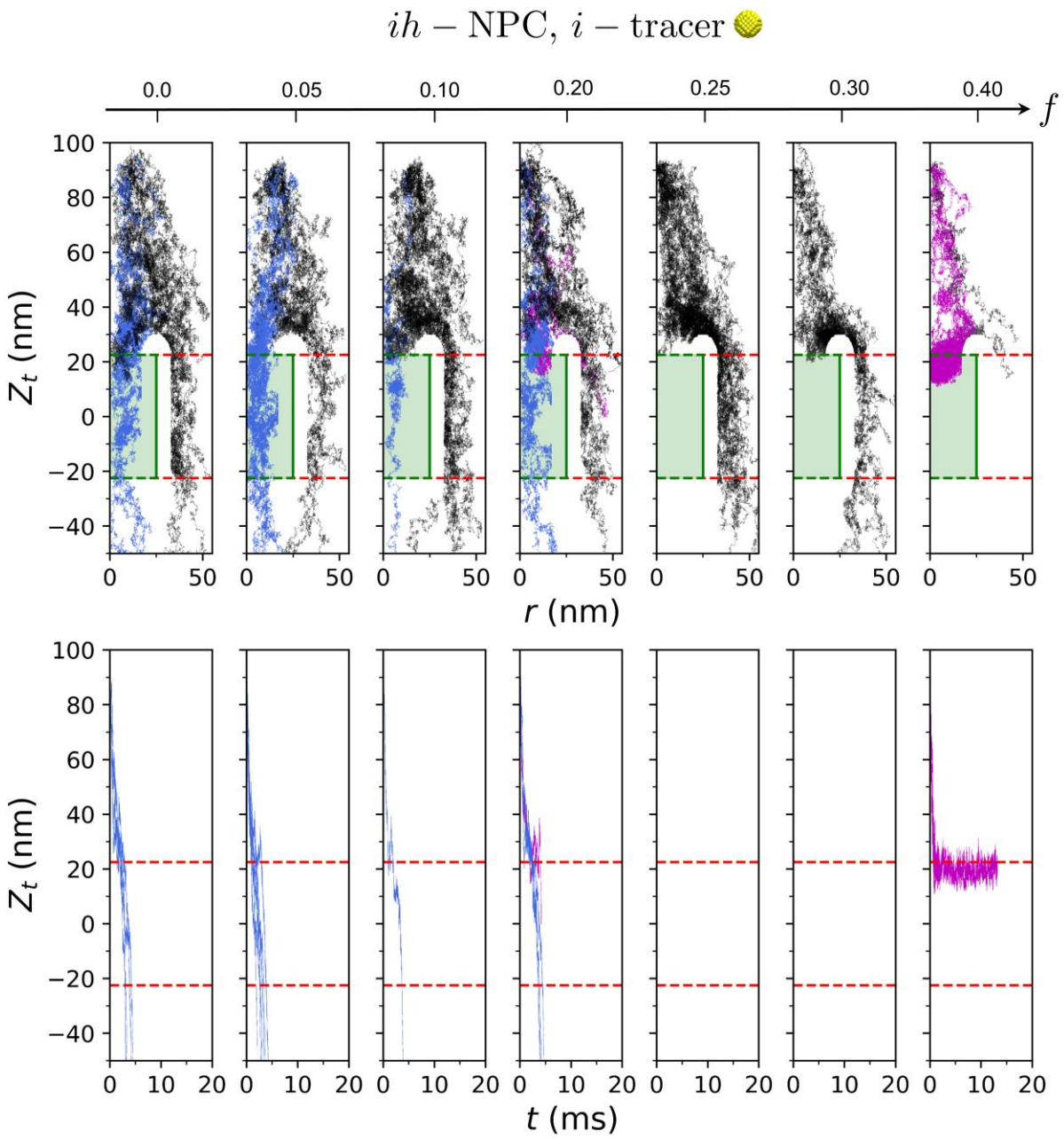

Figure S8. Inert patchy tracer trajectories from twenty independent simulations through inhomogeneous pore shown for different values of f (A) Tracer paths during the simulations represented as Z_t vs r plots, where Z_t is the z-coordinate of the tracer, and r is tracer radial coordinate. (B) Plots showing the variation of Z_t with time t.

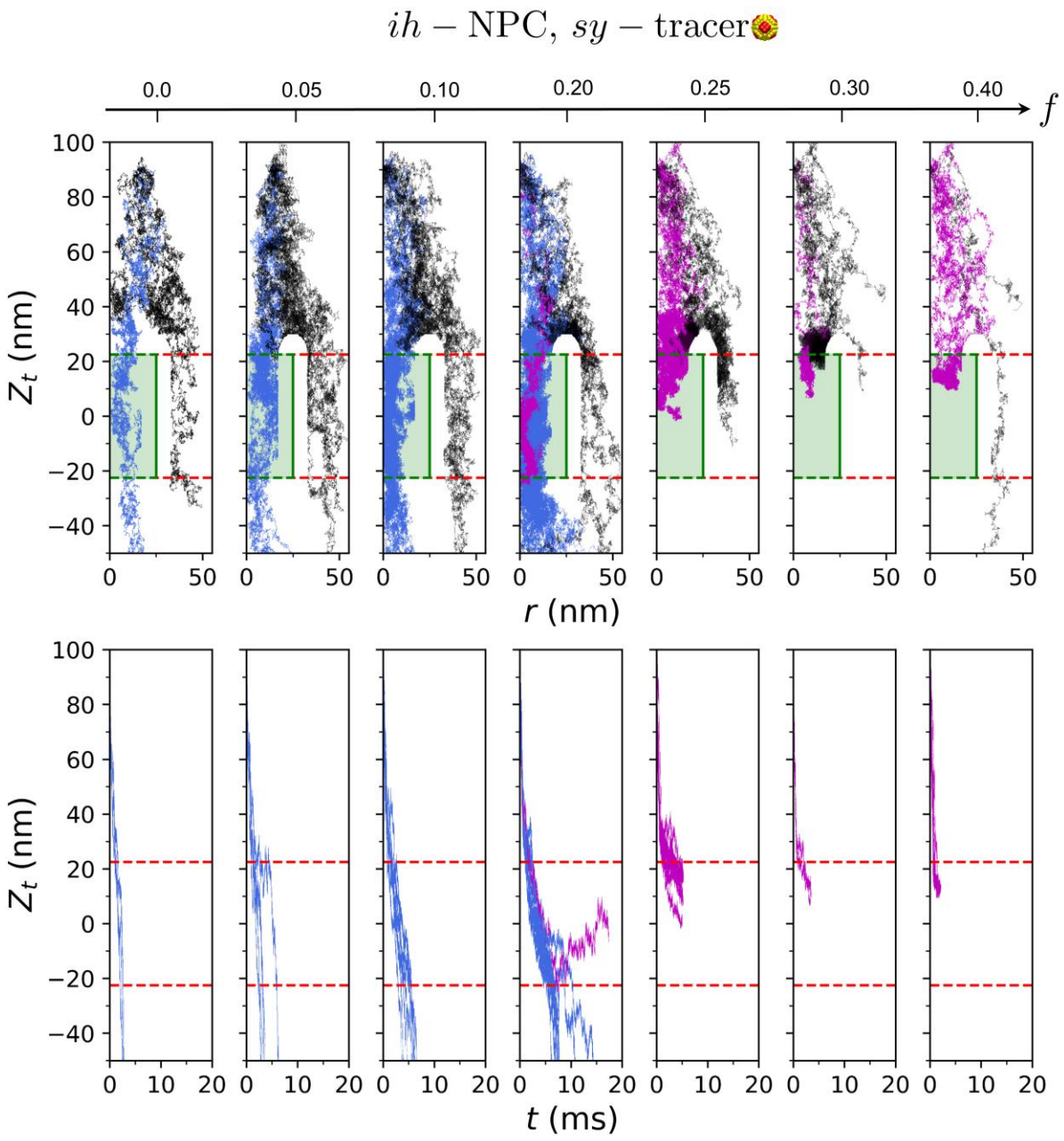

Figure S9. Distributed patchy tracer trajectories from twenty independent simulations through inhomogeneous pore shown for different values of f (A) Tracer paths during the simulations represented as Z_t vs r plots, where Z_t is the z-coordinate of the tracer, and r is tracer radial coordinate. (B) Plots showing the variation of Z_t with time t.

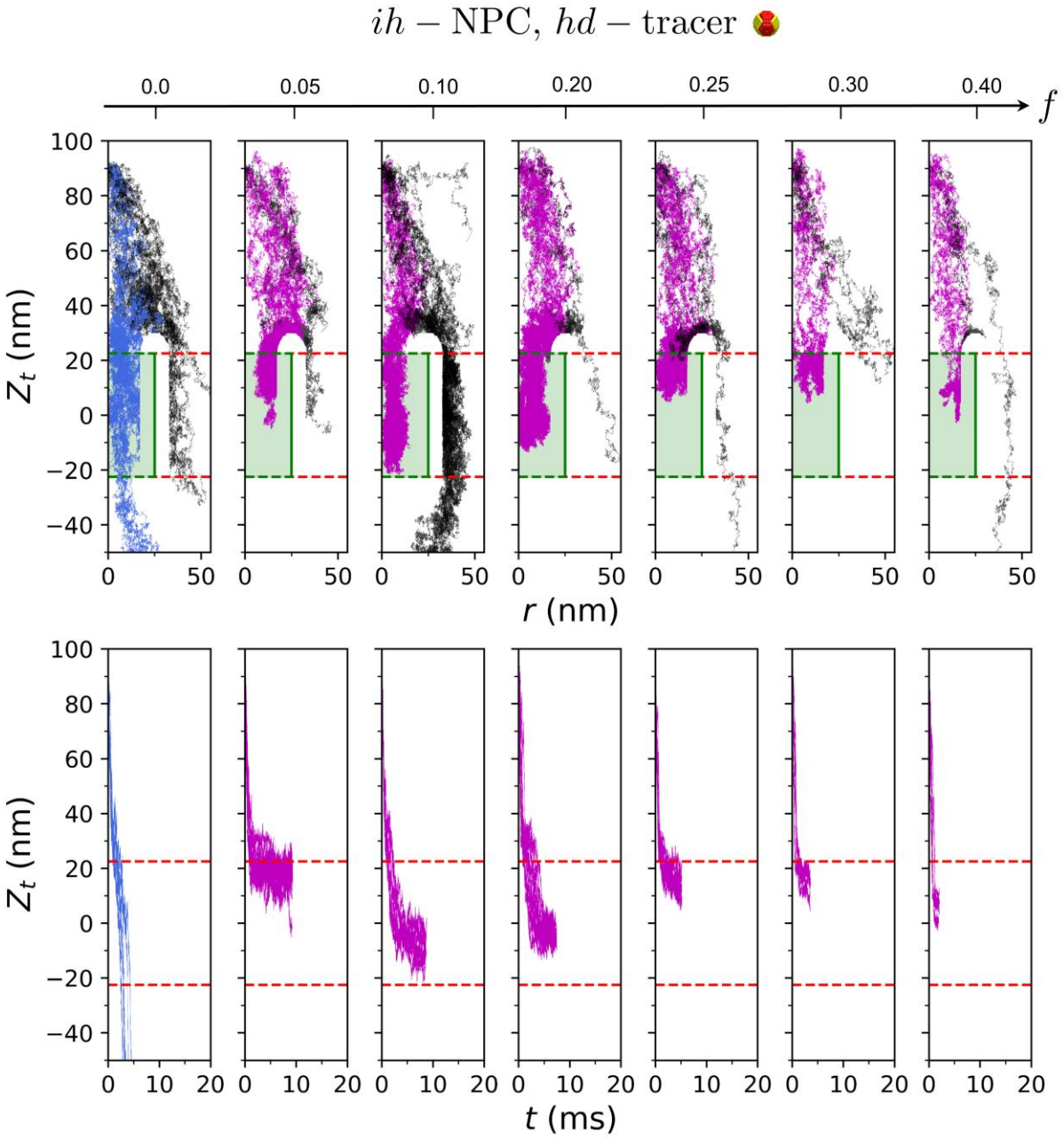

Figure S10. Dense patchy tracer trajectories from twenty independent simulations through inhomogeneous pore shown for different values of f (A) Tracer paths during the simulations represented as Z_t vs r plots, where Z_t is the z-coordinate of the tracer, and r is tracer radial coordinate. (B) Plots showing the variation of Z_t with time t.

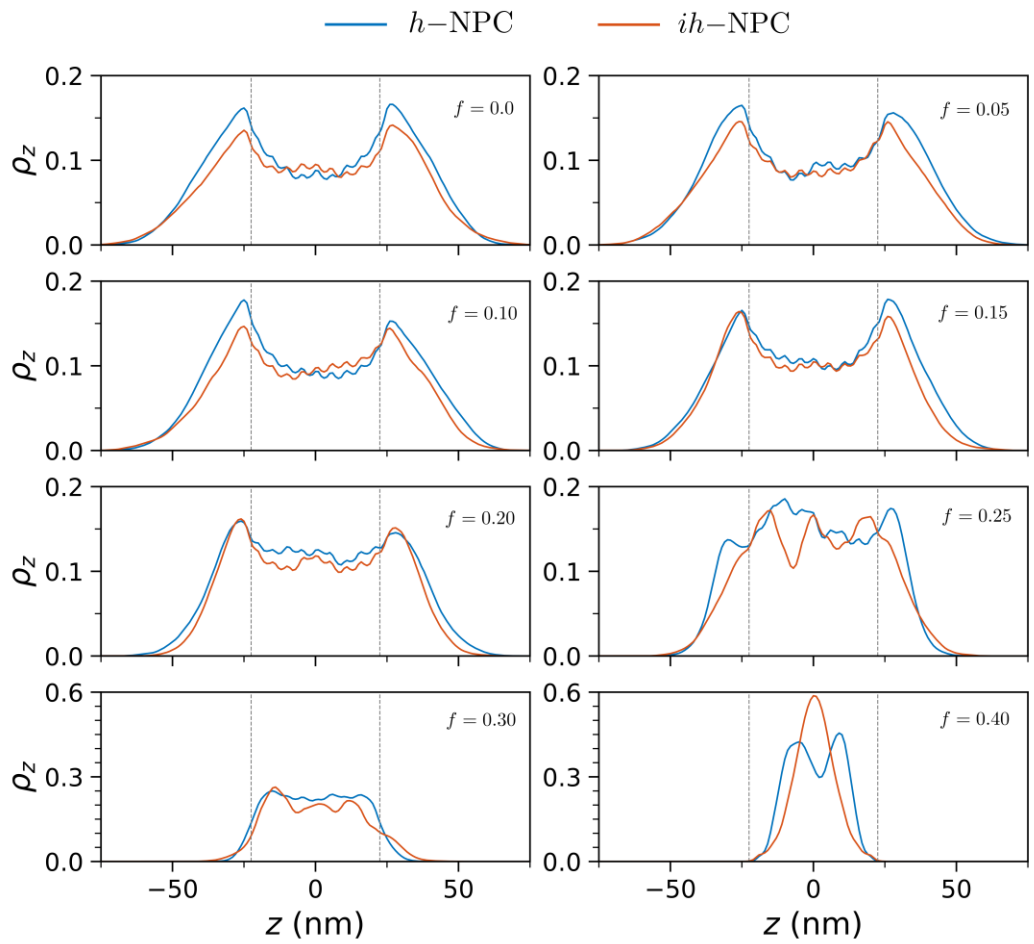

Figure S11. Plots showing the equilibrated density distributions of polymer brush segments, considering both hydrophobic and hydrophilic segments. The density distributions are calculated for the full pore by considering the all nine rings of the polymer brushes, plotted along the axial direction of the NPC.

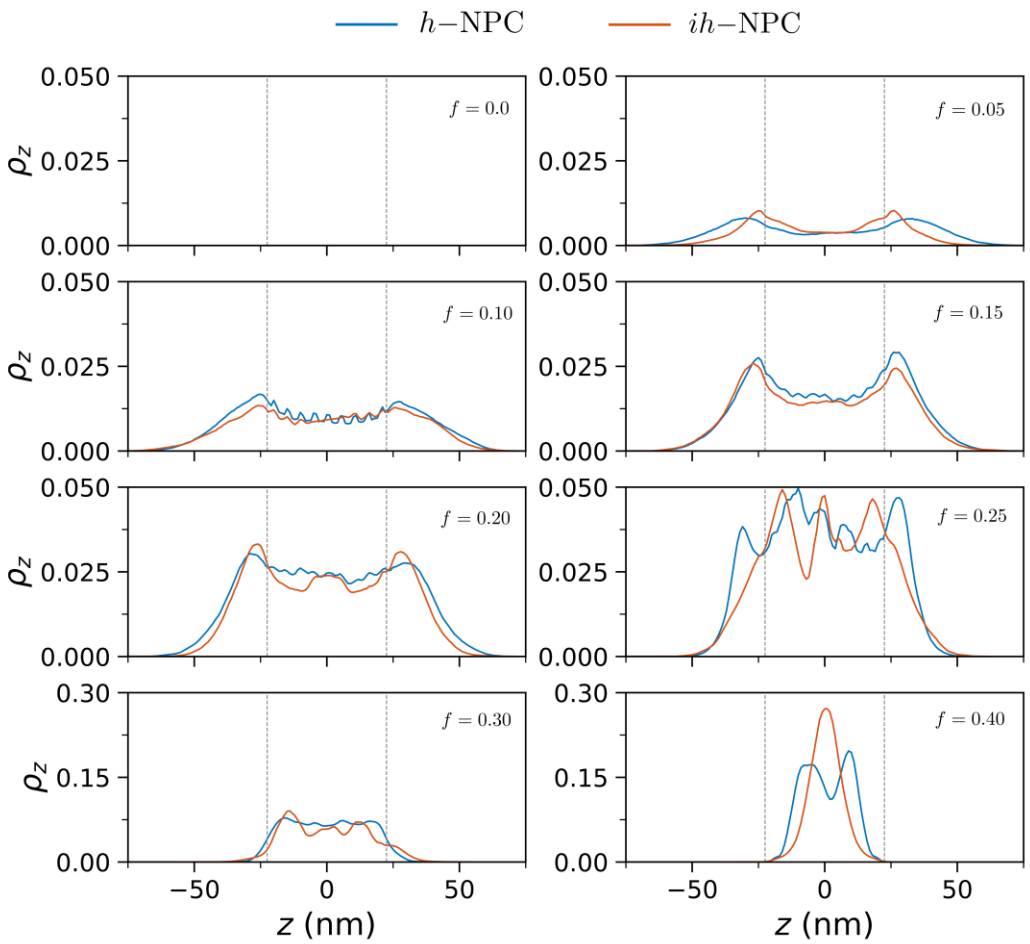

Figure S12. Plots showing the equilibrated density distributions of polymer brush segments, considering only hydrophilic segments. The density distributions are calculated for the full pore by considering the all nine rings of the polymer brushes, plotted along the axial direction of the NPC.

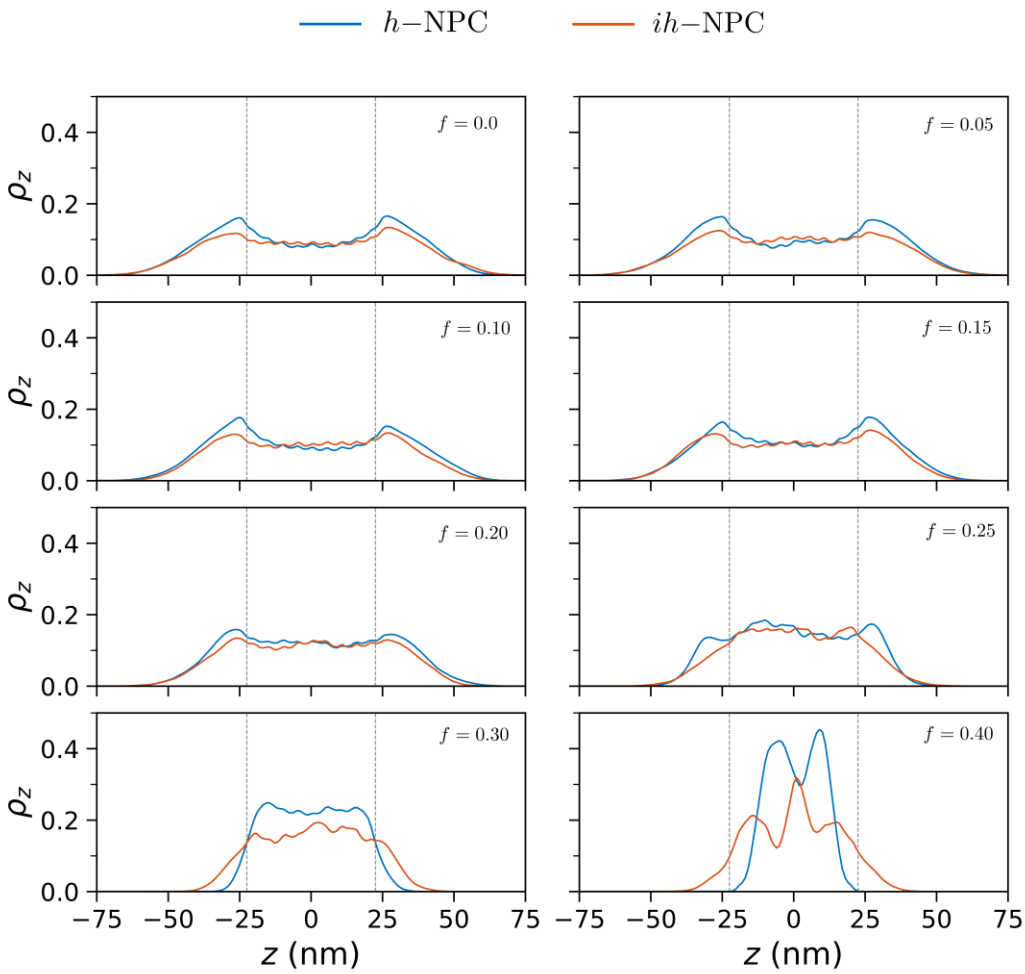

Figure S13. Plots showing the equilibrated density distributions of polymer brush segments, considering both hydrophobic and hydrophilic segments. The density distributions are calculated by considering only the middle three rings of the polymer brushes, plotted along the axial direction of the NPC.

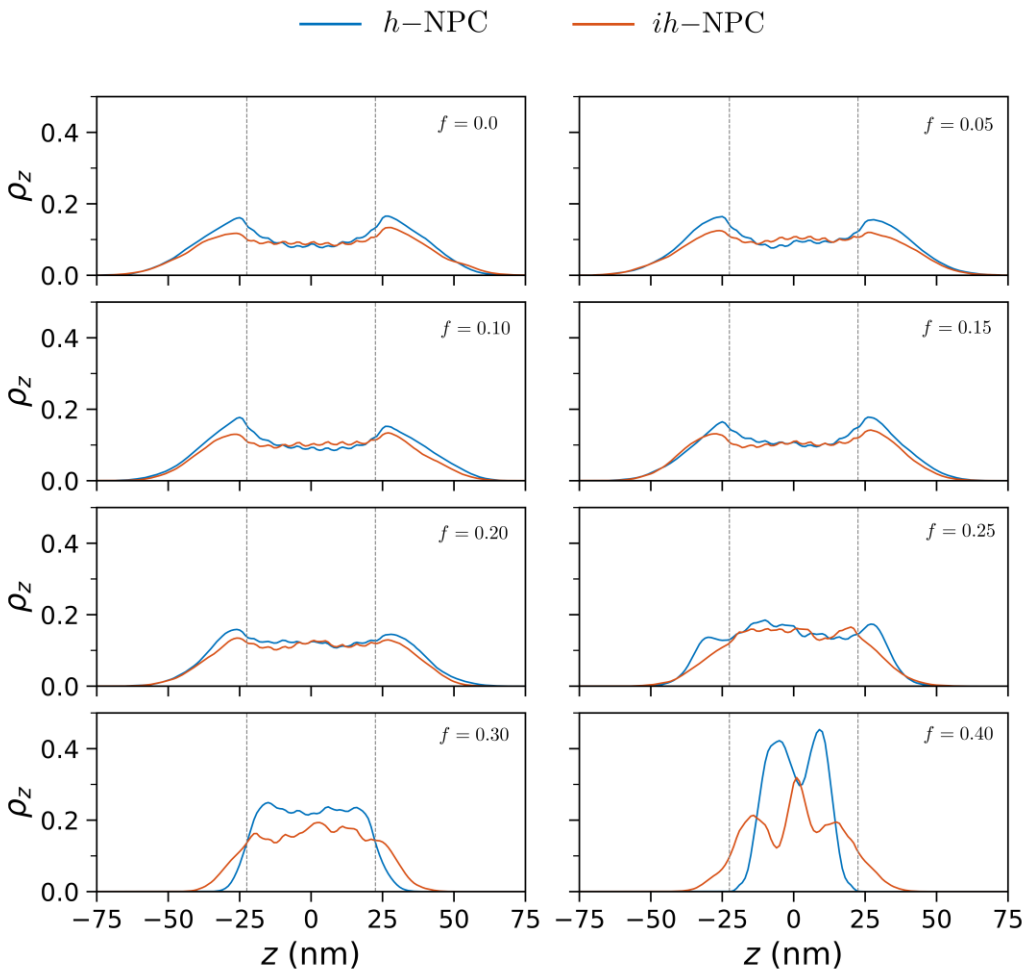

Figure S14. Plots showing the equilibrated density distributions of polymer brush segments, considering only hydrophilic segments. The density distributions are calculated for the full pore by considering only the middle three rings of the polymer brushes, plotted along the axial direction of the NPC.

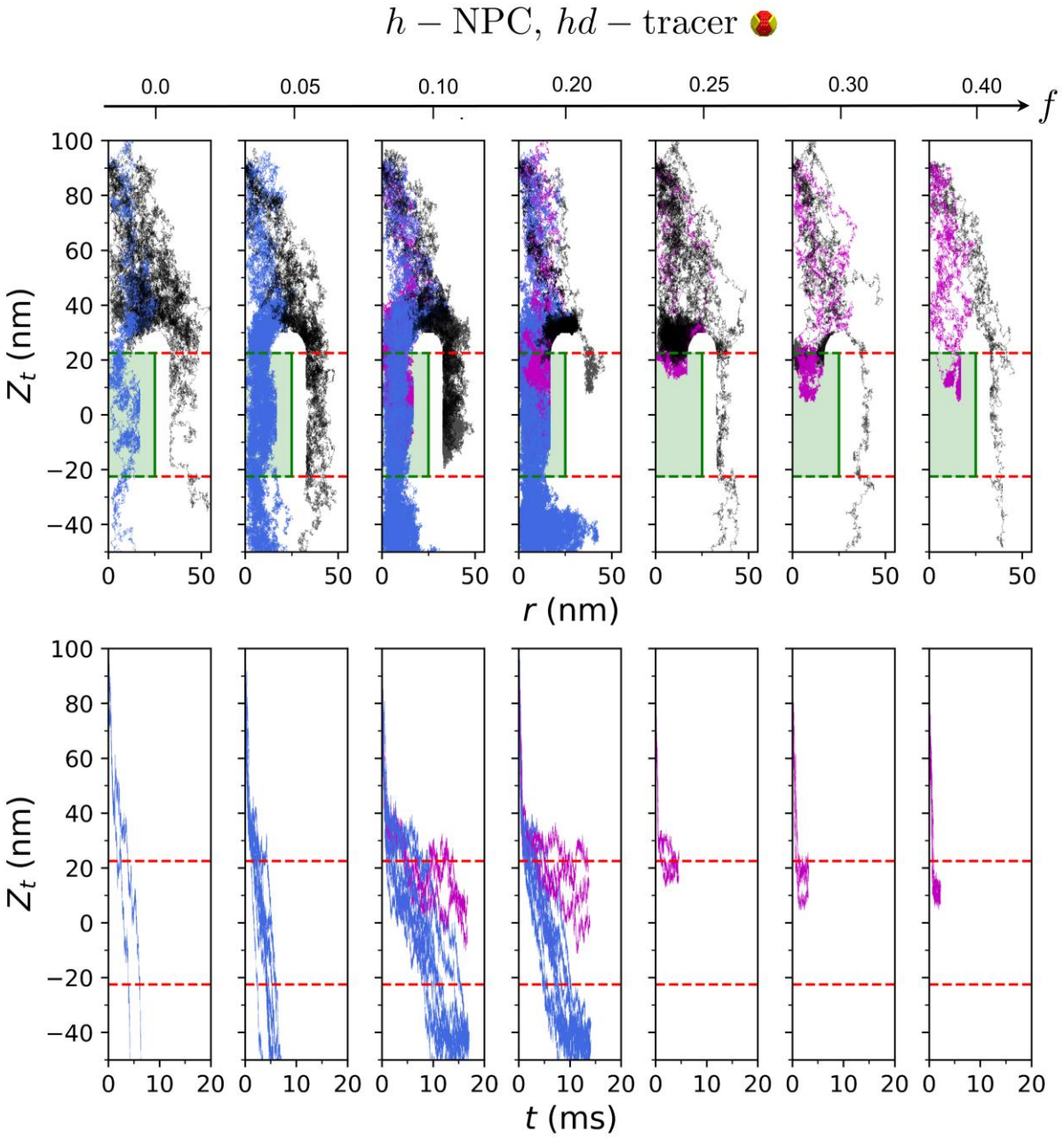

Figure S15. Denser patchy tracer trajectories from twenty independent simulations through homogeneous pore shown for different values of f after weakening of tracer-FG hydrophobic affinity (A) Tracer paths during the simulations represented as Z_t vs r plots, where Z_t is the z-coordinate of the tracer, and r is tracer radial coordinate. (B) Plots showing the variation of Z_t with time t.

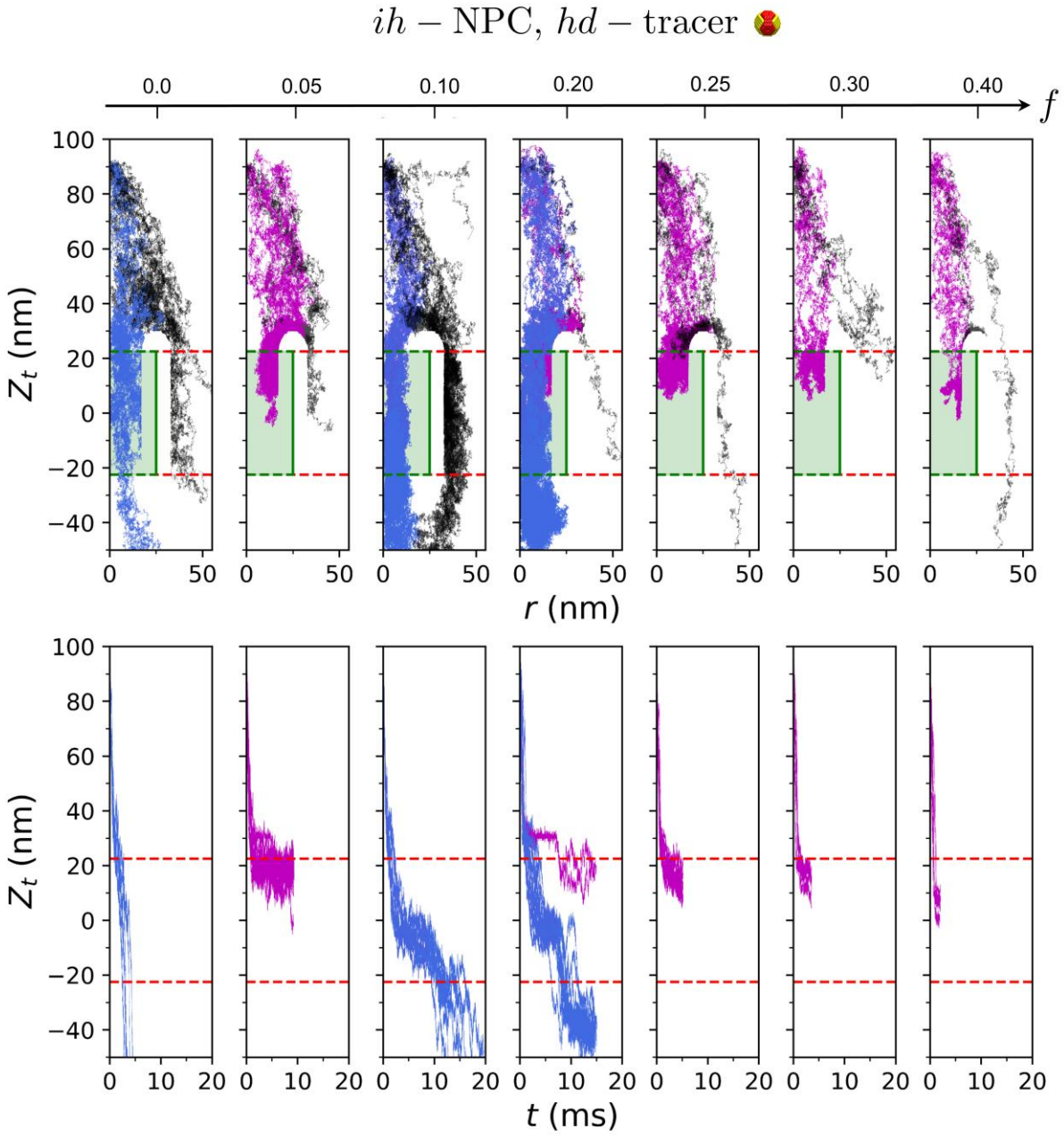

Figure S16. Dense patchy tracer trajectories from twenty independent simulations through inhomogeneous pore shown for different values of f after weakening of tracer-FG hydrophobic affinity (A) Tracer paths during the simulations represented as Z_t vs r plots, where Z_t is the z-coordinate of the tracer, and r is tracer radial coordinate. (B) Plots showing the variation of Z_t with time t.

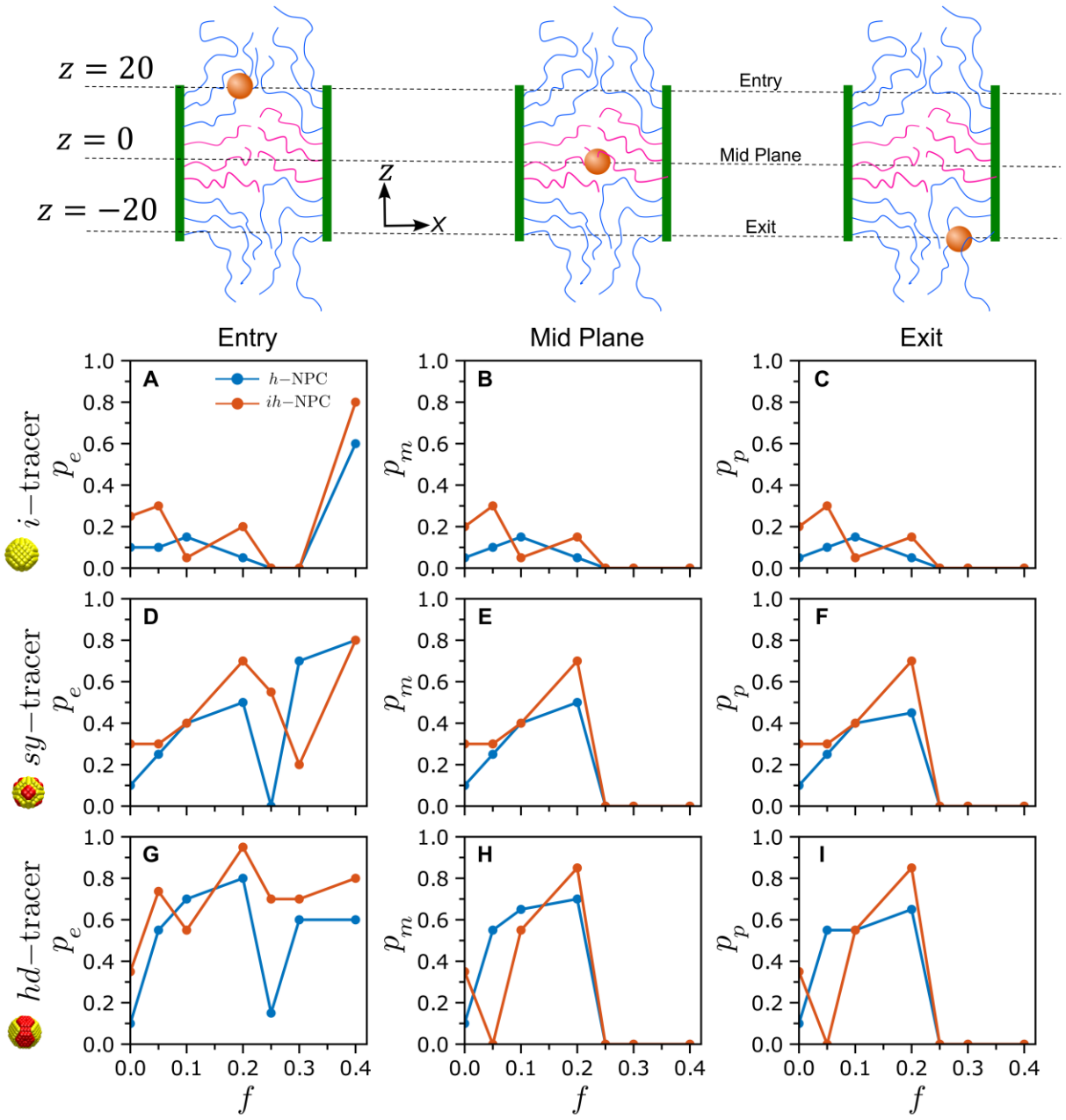

Figure S17. Final probabilities associated with different tracer translocation as function of f after weakening hydrophobic interaction between *hd*-tracer and middle rings, including the probability of tracer entry, p_e, probability of crossing the NPC mid-plane, p_m, and the probability of the tracer completely exiting the pore, p_p. Plots are shown for *i*-tracer (A – C), *sy*-tracer (D – F) and *hd*-tracer (G – I) corresponding to both h −NPC and ih −NPC.

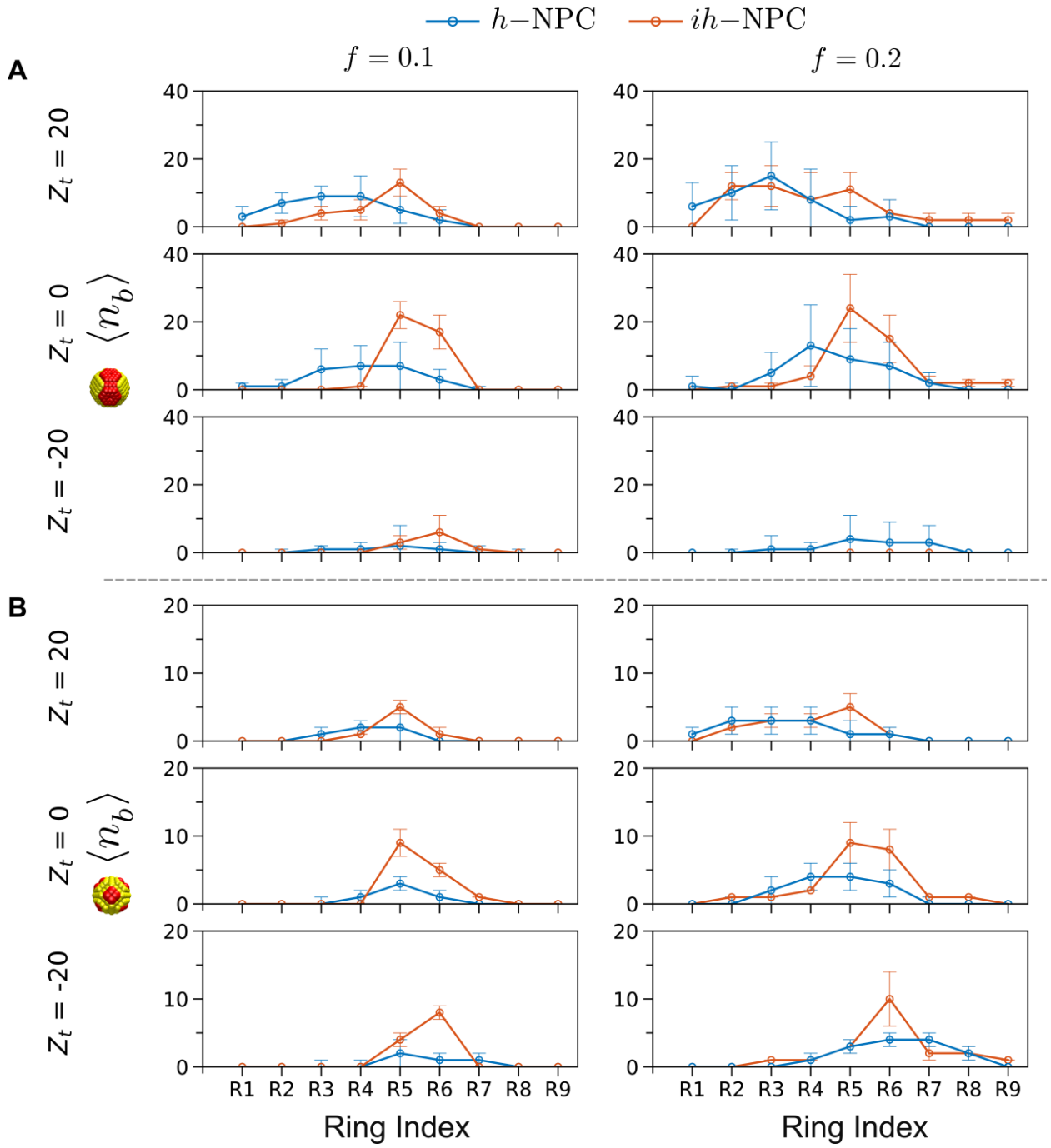

Figure S18. Average number of binding contacts, $\langle n_b \rangle$, between tracer binding domains and FG-repeats corresponding to individual rings, $R1 - R9$, shown for both *h*-NPC and *ih*-NPC at $f = 0.1$ and $f = 0.2$. The variation in $\langle n_b \rangle$ with respect to the ring index are shown at the entry ($Z_t = 20$), mid-plane ($Z_t = 0$) and exit ($Z_t = -20$) of the NPCs for (A) *hd*-tracer and (B) *sy*-tracer.

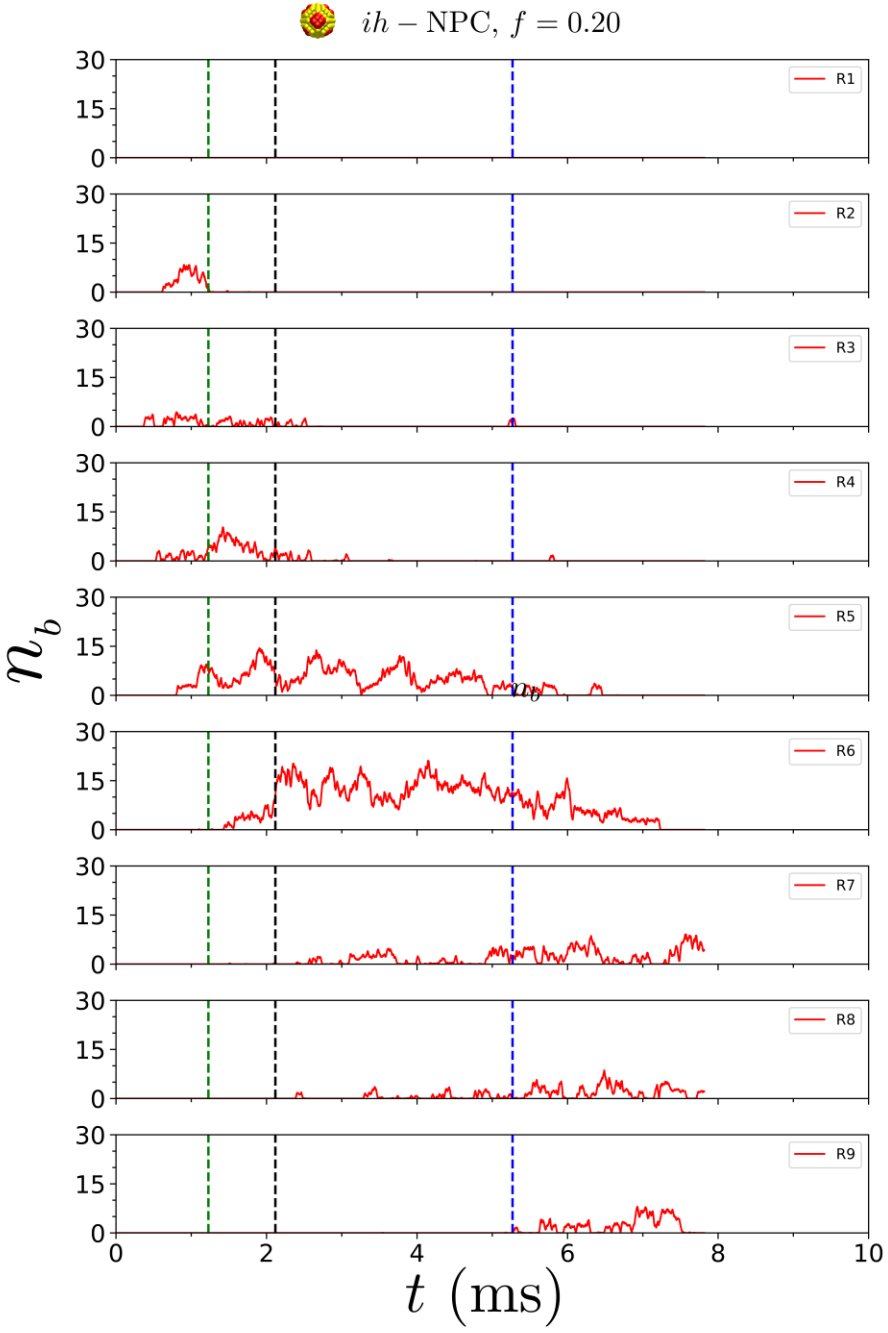

Figure S19. Hydrophobic binding contacts between the *sy*-tracer (distributed patchy tracer) and FG-Nups at $f = 0.2$, during its passage through the *ih*-NPC (inhomogeneous pore). The tracer is sequentially handed over from one FG-Nup to another as it enters and moves downwards through the pore.

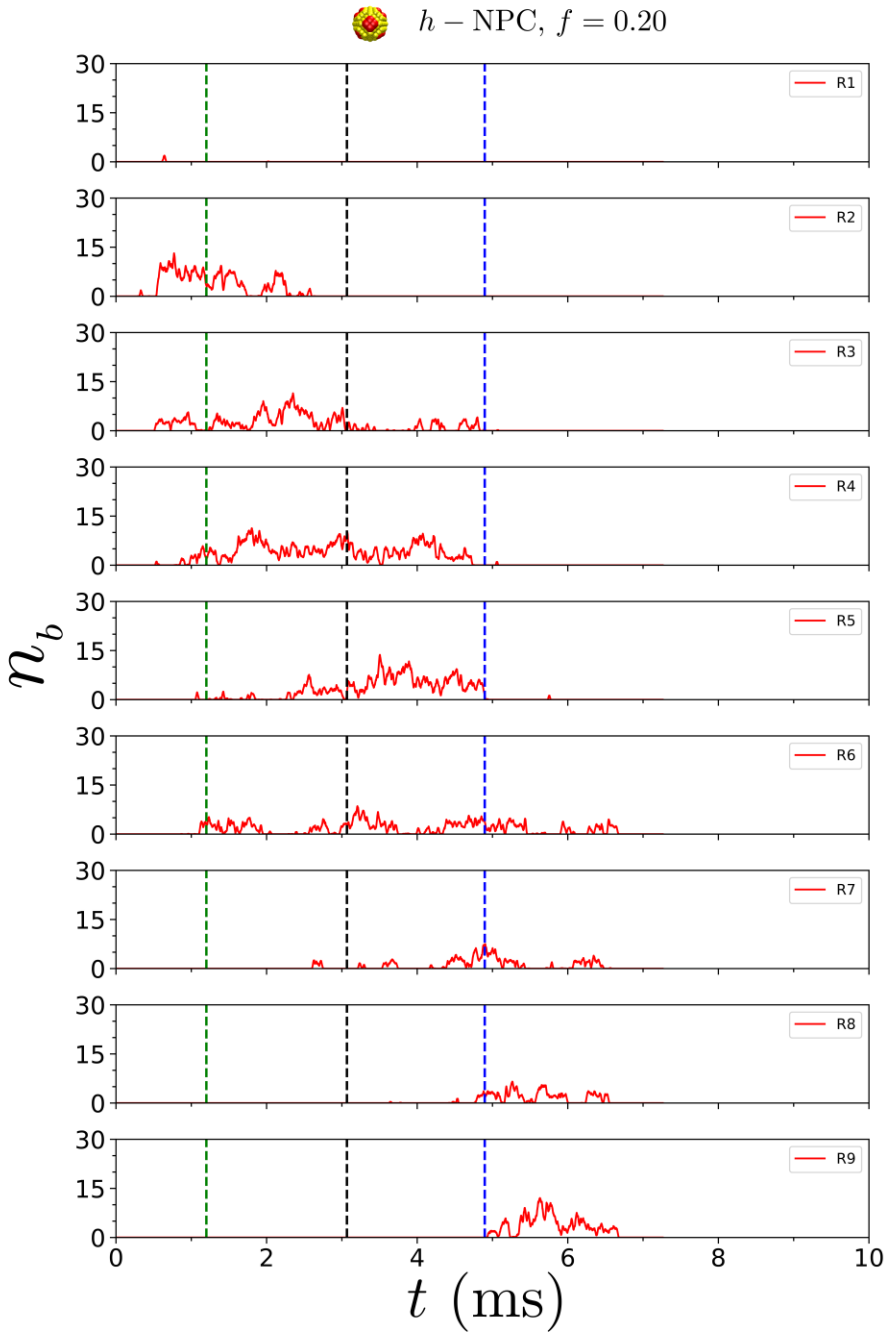

Figure S20. Hydrophobic binding contacts between the *sy*-tracer (distributed patchy tracer) and FG-Nups at $f = 0.2$, during its passage through the *h*-NPC (homogeneous pore). The tracer is sequentially handed over from one FG-Nup to another as it enters and moves downwards through the pore.

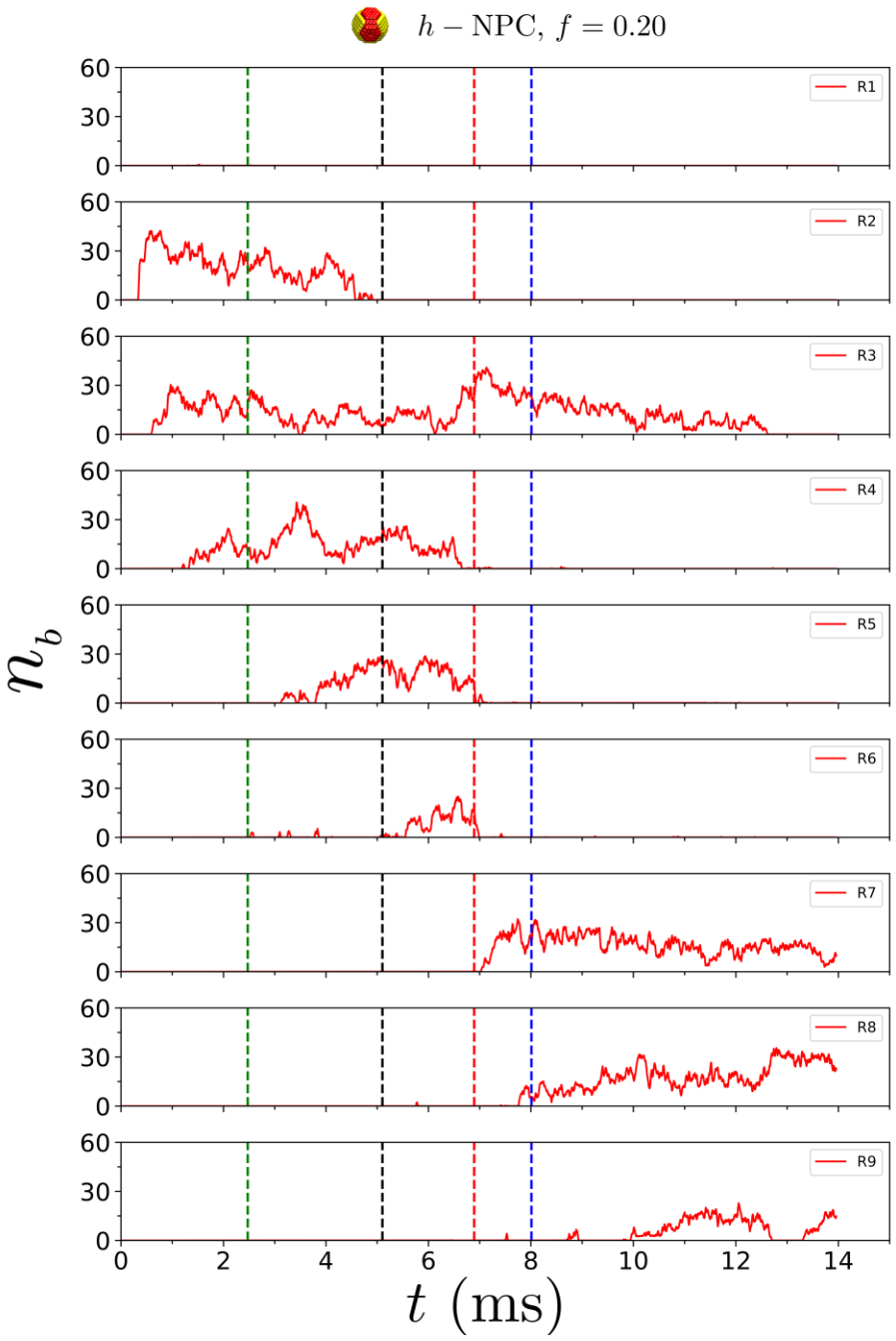

Figure S21. Hydrophobic binding contacts between the *hd*-tracer (denser patchy tracer) and FG-Nups at $f = 0.2$, during its passage through the *h*-NPC (homogeneous pore). The tracer is sequentially handed over from one FG-Nup to another as it enters and moves downwards through the pore.